Fusion of deformed nuclei in the reactions of $^{76}Ge+^{150}Nd$ and $^{28}Si+^{198}Pt$ at the Coulomb barrier region

K. Nishio,[1] H. Ikezoe,[1] S. Mitsuoka,[1] and J. Lu[2]
[1]*Advanced Science Research Center, Japan Atomic Energy Research Institute, Tokai-mura, Ibaraki 319-1195, Japan*
[2]*Institute of Modern Physics, Chinese Academy of Sciences, 730000 Lanzhou, China*
(Received 17 December 1999; published 30 May 2000)

Evaporation residue cross sections for $^{28}Si+^{198}Pt$ and $^{76}Ge+^{150}Nd$, both of which form a compound nucleus ^{226}U, were measured in the vicinity of the Coulomb barrier. The measurement gives direct evidence that the system really fuses together to form a fully equilibrated compound nucleus. For the $^{28}Si+^{198}Pt$ reaction, we have measured the fission fragments to determine the fusion cross section by taking advantage of the highly fissile character of ^{226}U. The evaporation residue cross section and the fusion cross section for $^{28}Si+^{198}Pt$ allowed us to investigate the deexcitation process (exit channel) of the compound nucleus ^{226}U, and the parameters entering in a statistical model calculation could be determined. By estimating the deexcitation of the compound nucleus ^{226}U with the statistical model, the effect of the deformed nucleus ^{150}Nd on the fusion reaction $^{76}Ge+^{150}Nd$ was extracted. The experimental data indicated that there is more than 13 MeV extra-extra-push energy for the system to fuse together when the projectile ^{76}Ge collides at the tip of the deformed ^{150}Nd nucleus. On the contrary, for the side collision which is more compact in configuration than the tip collision, no fusion hindrance is suggested.

PACS number(s): 25.60.Pj, 25.70.Jj, 24.60.Dr

I. INTRODUCTION

Synthesis of a superheavy element (SHE) is one of the important topics in nuclear physics because it gives insight into the shell stabilization in the vicinity of the double magic nucleus of $Z=114$ and $N=184$, without which such a heavy nucleus cannot exist due to the overwhelming repulsive Coulomb force. Recently, an evidence of producing a new SHE was reported. A successive α-decay chain was observed by hot-fusion reaction of $^{48}Ca+^{244}Pu$ [1], which was attributed to the decay of the element 114. The Berkeley group reported the observation of the three decay chains starting from $Z=118$ [2] and consisting of six subsequent α decays. Among these α-decay nuclei they have observed, there is no nuclei whose decay properties (energy and lifetime) are known. Therefore, further experimental study of synthesizing SHEs and measuring its α-decay properties is necessary.

The production cross section of SHEs using hot- and cold-fusion reaction is extremely low, i.e., picobarn range, making an investigation of SHEs very difficult. Other approaches of synthesizing a SHE proposed theoretically are a gentle fusion [3] and a hugging fusion [4] which use deformed nuclei as colliding partners. In these cases, there is a certain probability that the deformed target and projectile collide with each other with their symmetry axis being orthogonal. Since this configuration is compact at touching, the dynamical fusion process starting from this specific configuration may proceed to form a compound nucleus with larger probability than the other configurations.

The effects of nuclear deformation on the fusion process have been investigated in reactions using light projectile beams. This is seen in reactions using a deformed target such as ^{154}Sm [5,6], where the fusion barrier height varies with colliding angle and hence the barrier height distributes widely around the spherical Coulomb barrier. It leads to a substantial enhancement of fusion cross section in the region below the spherical Coulomb barrier compared to the calculation of the one-dimensional barrier penetration model which assumes a spherical nuclear shape. Coupling to the inelastic channels also enhances the sub-barrier fusion cross section [5–7]. This fusion model is based on the idea that the colliding systems are bound to amalgamate with each other when they overcome or penetrate the fusion barrier. On the contrary, in the reaction of a heavy target-projectile combination leading to a heavy and fissile compound nucleus, to overcome the fusion barrier alone is not enough to form a compound nucleus. The system must overcome the saddle point of the compound nucleus, which is located inside the fusion barrier between the heavy target and projectile. In order to drive the system over the saddle point, additional energy is needed, which is called the extra-extra-push energy E_{XX}. If the system cannot overcome the saddle point, it breaks as quasifission after a significant amount of nucleon transfer and kinetic energy loss. The appearance of quasifission makes the experimental identification of the complete fusion event ambiguous when one only measures the mass number and the kinetic energy of fission fragment. The ambiguity expands with increasing the mass symmetry and mass number of colliding nuclei. In order to get direct evidence of fusion, detecting the evaporation residues is essential.

The extra-extra-push energy increases quite rapidly with increasing an effective fissility parameter χ_{eff} [8] in the region of $\chi_{\mathrm{eff}} > \sim 0.75$ The sharp increase of E_{XX} is attributed to the damping of the kinetic energy in the course of dynamical evolution. The distance between the fusion barrier position and the true saddle point increases with the mass of the interacting nuclei. It might result in a significant loss of mutual kinetic energy during the course of fusion process. Let us consider the case of a reaction using a prolately deformed target and a spherical projectile with their effective fissility parameter being close to or larger than the threshold χ_{eff}

$=0.75$. The distance between the mass centers of two nuclei at the touching configuration varies with the colliding angle with respect to the symmetric axis of deformed target $\theta_{\rm coll}$ and reaches a maximum at the tip collision. In this case, the $E_{\rm XX}$ may be larger at the tip collision than at the side collision.

The effects of target deformation on fusion process in the massive target-projectile combination were investigated by Mitsuoka *et al.* [10]. By measuring the cross section of the evaporation residue for the reaction of ^{60}Ni$+^{154}$Sm ($\chi_{\rm eff}=0.735$), they found that an extra-extra-push energy of about 20 MeV is required for the system to form a compound nucleus when ^{60}Ni collides at the tip of the deformed ^{154}Sm and additional energy is not needed for the side collision.

In this paper we have carried out the measurement of the evaporation residue cross section in the reactions of ^{76}Ge $+^{150}$Nd ($\chi_{\rm eff}=0.749$) and ^{28}Si$+^{198}$Pt ($\chi_{\rm eff}=0.584$), both of which form the same compound nucleus ^{226}U. The system ^{76}Ge$+^{150}$Nd has a slightly larger value of $\chi_{\rm eff}$ compared to ^{60}Ni$+^{154}$Sm, and we expect a fusion hindrance, depending on the colliding angle. We have also measured the fission cross sections for the reaction of ^{28}Si$+^{198}$Pt to estimate the fusion cross section. No extra-extra-push energy is expected for the fusion of this system because of the small $\chi_{\rm eff}$ value. In this system, we can fix the parameters used in a statistical model calculation by comparing the measured evaporation residue (ER) cross sections with the calculations. After this, we can extract the fusion probability of ^{76}Ge$+^{150}$Nd at the sub-barrier energy region by comparing the measured ER cross section and the results of the statistical model calculation for the decay of the compound nucleus ^{226}U, assuming the deexcitation is well simulated by the statistical model.

In Sec. II we describe the experimental setup followed by data analysis in Sec. III. The calculations and discussion will be given in Sec. IV. We give in Sec. V a summary and some concluding remarks.

II. EXPERIMENTAL SETUP

A. Measurement of the fission cross section for ^{28}Si$+^{198}$Pt

The fission cross section for ^{28}Si$+^{198}$Pt was determined by measuring the angular distribution of fission fragments. The experimental arrangement is shown in Fig. 1. Beams of ^{28}Si having energy of 131.7–190.3 MeV were supplied by the JAERI-tandem accelerator and used to irradiate the ^{198}Pt target. Typical beam current was 10–70 *e* nA. The target of 195 μg/cm^2 thickness was prepared by sputtering the enriched material (98%) of ^{198}Pt isotopes on a 30 μg/cm^2 thick carbon foil. The target was tilted at 30° to the beam axis with the carbon backing facing the downstream of the beam. A ΔE-E ionization chamber was used to measure the fission fragments. It consists of a position-sensitive silicon detector (PSD) and an ionization chamber, which are mounted in the stainless steel container (see Fig. 1). The PSD has an active area of 34.0 mm length $\times$ 2.5 mm width. The ionization chamber is operated with 20 ± 1 Torr isobutane under gas flow condition. Two ΔE-E ionization chambers were mounted on both sides of the target. The acceptance angle of

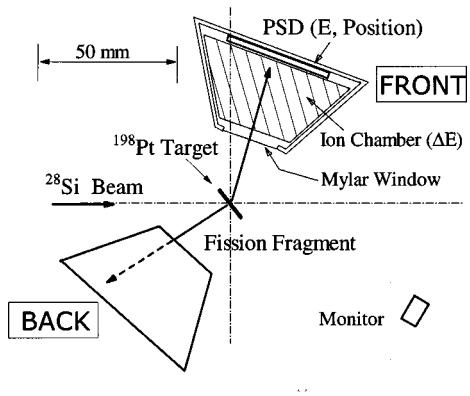

FIG. 1. Experimental arrangement for the measurement of fission fragment angular distribution for ^{28}Si$+^{198}$Pt.

the detector was $64°\leqslant\varphi_{\rm LAB}\leqslant92°$ for the front side detector and $129°\leqslant\varphi_{\rm LAB}\leqslant156°$ for the back side detector. A silicon surface barrier detector was used to monitor elastic scattering at forward angle of 40° for the cross section normalization.

B. Measurement of the evaporation residue cross section for ^{28}Si$+^{198}$Pt and ^{76}Ge$+^{150}$Nd

Measurement of the evaporation residue cross sections following the fusion of ^{28}Si$+^{198}$Pt and ^{76}Ge$+^{150}$Nd was made by using ^{28}Si and ^{76}Ge beams supplied by the JAERI-tandem booster facility. The beam energy $E_{\rm beam}$ was varied to measure the excitation functions of ER cross sections as listed in Table I (^{28}Si$+^{198}$Pt) and Table II (^{76}Ge$+^{150}$Nd). In these tables the c.m. energy in a parentheses is determined at the half-depth in the target layer. The integrated beam dose supplied is also listed in these tables. The targets were made by sputtering the enriched material on a 0.8 μm thick aluminum foil. The thickness of the ^{198}Pt (enrichment of 98%) and ^{150}Nd (Nd_2O_3, enrichment of 92.5%) targets was 460 μg/cm^2 and 380 μg/cm^2, respectively.

The evaporation residues emitted to the beam direction were separated in flight from the primary beams by the JAERI recoil mass separator (JAERI-RMS) [11]. Before entering the recoil mass separator, the ER's charge state was reset by passing through a 30 μg/cm^2 carbon foil (charge reset foil). The separated recoils were implanted into a double sided position-sensitive strip detector (DPSD, 73 $\times$55 mm^2). Two larger area timing detectors, one positioned at the front of the DPSD and the other 30 cm upstream of the DPSD, were used to obtain the time-of-flight (TOF) signal of incoming particles. The timing detector consists of a microchannel plate detector that detects electrons ejected when the incoming particle passes through a gold plated Formvar foil. The presense of a timing signal in the TOF detectors was used to separate ER implant events from the subsequent α decays, which generate no TOF signals. A two-dimensional spectrum of the energy versus TOF gives a rough estimate of the mass number of the incoming particle. A clock signal was recorded at the moment of the event occurrence to reconstruct the time interval between the successive α-decay events. Alpha-decay events longer than 5 μs life were re-

TABLE I. Integrated beam dose supplied for the measurement of evaporation residue cross sections for ^{28}Si+^{198}Pt reaction. $E_{\rm beam}$ ($E_{\rm c.m.}$) is the beam energy (c.m. energy) in MeV units. Cross sections in nb for evaporation residues of (a) ^{223}U+^{219}Th+^{215}Ra, (b) ^{222}U+^{218}Th +^{214}Ra, (c) ^{221}U+^{217}Th, (d) ^{220}U+^{216}Th, (e) ^{220}Pa+^{216}Ac, (f) ^{219}Pa+^{215}Ac, (g) ^{222}Pa, and (h) ^{221}Th are listed.

$E_{\rm beam}$ ($E_{\rm c.m.}$)	Particles	(a)	(b)	(c)	(d)	(e)	(f)	(g)	(h)
140.0 (120.0)	17.8×10^{15}	42±26	36±22	-	-	-	-	-	-
142.7 (122.5)	8.8×10^{15}	124±72	85±52	-	-	-	-	5^{+10}	-
145.6 (125.0)	5.5×10^{15}	100±63	62^{+47}_{-40}	24^{+31}_{-21}	-	-	-	6^{+13}	-
148.4 (127.5)	6.2×10^{15}	129±76	146±83	20^{+26}_{-17}	-	-	-	16^{+17}_{-12}	-
151.3 (130.0)	7.3×10^{15}	236±130	277±150	29^{+29}_{-21}	-	-	-	16^{+16}_{-11}	-
154.0 (132.5)	8.6×10^{15}	100±57	443±230	97±56	11^{+14}_{-9}	-	-	11^{+11}_{-8}	-
156.9 (135.0)	3.8×10^{15}	162±100	487±260	512±280	51^{+52}_{-38}	25^{+32}_{-24}	-	11^{+22}	-
159.7 (137.5)	7.1×10^{15}	147±82	484±250	510±260	7.3^{+15}	32^{+24}_{-20}	-	-	-
162.6 (140.0)	4.7×10^{15}	94^{+72}_{-61}	443±240	606±320	29^{+39}_{-25}	21^{+27}_{-18}	-	-	-
165.4 (142.5)	4.6×10^{15}	65^{+53}_{-44}	546±290	770±400	86^{+61}_{-53}	18^{+23}_{-15}	-	-	8^{+15}
168.2 (145.0)	4.7×10^{15}	102±64	690±360	860±440	225±130	68^{+45}_{-40}	13^{+16}_{-11}	-	-
171.0 (147.5)	4.2×10^{15}	78^{+64}_{-52}	683±360	855±450	412±220	42^{+37}_{-27}	9^{+18}_{-10}	-	-
173.9 (150.0)	3.6×10^{15}	108^{+78}_{-68}	1200±620	1138±590	907±470	143±83	71±45	-	-
176.7 (152.5)	4.9×10^{15}	26^{+27}_{-20}	636±330	633±330	652±340	135±73	61±36	-	-
179.0 (155.0)	4.5×10^{15}	29^{+37}_{-25}	643±340	237±140	501±270	210±120	99±59	-	-

corded for ^{28}Si+^{198}Pt. For ^{76}Ge+^{150}Nd, the minimum lifetime recorded was 425 μs. The energy calibration of the DPSD was made using known α lines from ^{214}Ra(7.137 MeV), ^{215}Ra(8.700), and ^{216}Th(7.921) [15] which were produced in the present reactions. The gain stability of the detection system was carefully checked by exposing the DPSD detectors to α particles from a ^{241}Am source. Typical energy resolution of the DPSD was 75 keV [full width at half maximum (FWHM)].

A silicon surface barrier detector to monitor the elastic scattering was set at the 45° direction in the target chamber in order to normalize the ER cross sections.

III. EXPRIMENTAL RESULTS

A. Fission cross section for ^{28}Si+^{198}Pt

Examples of the ΔE-E spectrum observed in the fission detectors are shown in Fig. 2 for selected six detection angles. The corresponding beam energy $E_{\rm beam}$ is 190.3 MeV. The three spectra on the left side and those on the right side were, respectively, obtained from the front and the back detector. The fission events are clearly distinguished from other reaction products arising from elastic, inelastic, and deep-inelastic scatterings, and the example of the fission gate is indicated in the spectrum of $\varphi_{\rm LAB}=65.8°$.

TABLE II. Integrated beam dose supplied for the measurement of evaporation residue cross sections for ^{76}Ge+^{150}Nd reaction. $E_{\rm beam}$ ($E_{\rm c.m.}$) is the beam energy (c.m. energy) in MeV units. Cross sections in nb for evaporation residues of (a) ^{223}U+^{219}Th+^{215}Ra, (b) ^{222}U +^{218}Th+^{214}Ra, (c) ^{221}U+^{217}Th, (d) ^{220}U+^{216}Th, (e) ^{220}Pa+^{216}Ac, (f) ^{219}Pa+^{215}Ac, (g) ^{222}Pa, and (h) ^{221}Th are listed. The last column shows the upper limit of the cross section, which is derived for the evaporation residue shown in parentheses.

$E_{\rm beam}$ ($E_{\rm c.m.}$)	Particles	(a)	(b)	(c)	(d)	(e)	(f)	(g)	(h)	Upper limit
288.8 (185.0)	2.5×10^{15}	-	-	-	-	-	-	-	-	3 (^{225}U)
296.3 (190.0)	2.4×10^{15}	-	-	-	-	-	-	-	-	4 (^{225}U)
305.6 (195.0)	4.7×10^{15}	-	-	-	-	-	-	-	-	4 (^{224}U)
320.5 (205.0)	1.9×10^{15}	-	-	-	-	-	-	-	-	8 (^{223}U)
324.3 (209.0)	3.0×10^{15}	8^{+10}_{-7}	3^{+5}	-	-	-	-	-	8^{+8}_{-6}	-
328.0 (211.5)	2.7×10^{15}	4^{+9}	3^{+6}	-	-	-	-	-	-	-
335.5 (215.0)	2.7×10^{15}	46±29	3^{+6}	-	-	-	-	-	-	-
343.0 (220.0)	1.7×10^{15}	129±73	19^{+17}_{-13}	-	-	-	-	15^{+15}_{-11}	-	-
350.4 (225.0)	2.1×10^{15}	74±44	35^{+23}_{-20}	12^{+25}	-	-	-	8^{+10}_{-7}	-	-
365.4 (235.0)	1.5×10^{15}	33^{+29}_{-23}	39^{+28}_{-24}	154±97	5^{+11}	-	-	-	-	-
370.9 (240.0)	0.5×10^{15}	43^{+45}_{-33}	302±160	544±310	183±100	-	-	-	-	-
378.4 (243.7)	3.5×10^{15}	3^{+7}	111±58	197±110	140±72	37^{+28}_{-24}	5^{+6}_{-4}	-	-	-
384.0 (247.5)	1.7×10^{15}	7^{+14}	116±63	158±96	225±120	61^{+50}_{-41}	38^{+26}_{-23}	-	-	-
390.1 (251.8)	1.8×10^{15}	6^{+13}	61±36	68^{+55}_{-45}	218±110	186±110	108±59	-	-	-

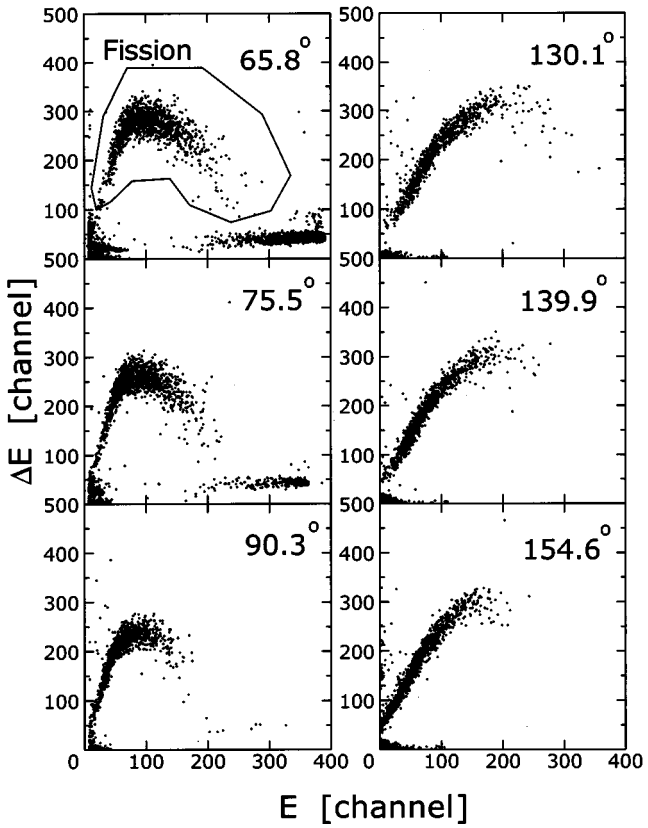

FIG. 2. Reaction products recorded on the ΔE-E plane at beam energy of 190.3 MeV for the ^{28}Si+^{198}Pt fission measurement. The laboratory angle φ_{LAB} is noted in each portion of the figure. Data on the left side (65.8°, 75.5°, and 90.3°) are obtained from the ΔE-E ionization chamber mounted on the downstream to the beam (front), whereas data on the right side (130.1°, 139.9°, and 154.6°) are obtained from that mounted on the upstream of the beam (back). The fission gate is indicated in the section of $\varphi_{\mathrm{LAB}}=65.8°$.

The differential fission cross section $d\sigma/d\Omega$ in the c.m. frame was obtained by applying the laboratory to the center-of-mass Jacobian to the cross section obtained in the laboratory system. In this process, the symmetric mass division was assumed and the total kinetic energy was predicted by the Viola systematic [12].

Figure 3 illustrates the fission cross section as a function of c.m. angle θ obtained at the beam energy of 190.3, 171.7, 148.9, and 135.2 MeV. The errors are estimated from the counting statistics and the uncertainty arising from extracting the fission events on the ΔE-E spectrum. The data points for a specific beam energy are fitted with

$$W(\theta)=A\sum_{I=0}^{\infty}(2I+1)T(I) \times \frac{\sum_{K=-I}^{I}\frac{1}{2}(2I+1)|d^{I}_{0,K}(\theta)|^2\exp(-K^2/K_0^2)}{\sum_{K=-I}^{I}\exp(-K^2/K_0^2)}, \quad (1)$$

which involves a summation over spin I and its projection K on the symmetry axis of the fissioning system. The variance of the K distribution, K_0^2, and the constant A are the adjustable free parameters. In this formula $d^I_{0,K}(\theta)$ stands for the symmetric top wave function, which was evaluated by applying the method described in [13]. We have calculated the transmission coefficient $T(I)$ for the partial wave I by using the CCDEF code [14]. In this fusion calculation the static deformations of the target and the projectile in addition to the couplings of inelastic excitations of the projectile and the target to the fusion process were taken into account. Details of the calculation will be given in the following section. The experimental data were fitted with Eq. (1) using a least-squares method, and the result is shown by the dashed curve in Fig. 3. We thus obtain the fission cross section by integrating the fitted curve over angle θ,

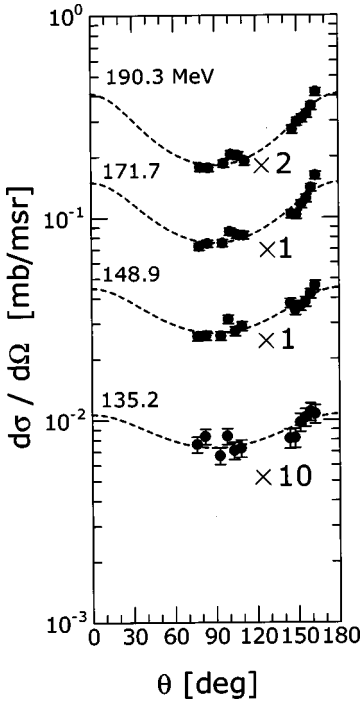

FIG. 3. Angular distributions of fission fragments obtained at $E_{\mathrm{beam}}=190.3$, 171.7, 148.9, and 135.2 MeV. The dashed curve is the best fit to the data obtained by varying K_0^2 and A in Eq. (1).

$$\sigma_{fiss}=2\pi\int_0^{\pi/2}W(\theta)\sin\theta d\theta, \quad (2)$$

and the results are shown in Fig. 4 (solid circles) and Table III as a function of c.m. energy. The error includes the statistical error and the systematic error of 15%. The curves in Fig. 4 are model predictions of the fusion cross section which will be explained in Sec. IV.

B. Evaporation residue cross section for ^{28}Si+^{198}Pt and ^{76}Ge+^{150}Nd

1. Particle identification

The evaporation residue cross section for a specific channel was determined by counting the ER-α_1 chain, where ER

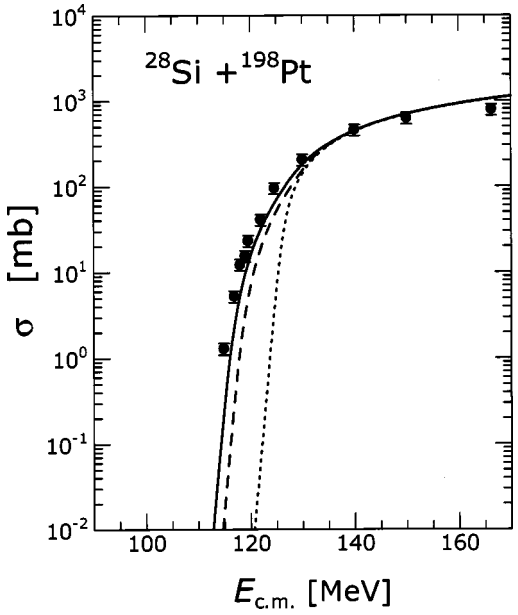

FIG. 4. Fission cross sections for ^{28}Si+^{198}Pt plotted as a function of $E_{c.m.}$ (solid circle with error bar). The dotted curve is the calculated fusion cross section based on the one-dimensional barrier penetrating model. The dashed curve is the result when the deformation effects of the projectile and the target are taken into account in the calculation. One obtains the solid curve when the couplings to the inelastic channels are additionally considered.

means the events produced when an incoming evaporation residue hits the DPSD and α_1 stands for the first α-decay observed. The kinetic energy and the time-of-flight information of the ER are also utilized in the analysis.

Figure 5 shows the typical two-dimensional spectrum of time of flight versus energy for particles detected in the focal plane detectors of the recoil mass separator for ^{76}Ge $+^{150}$Nd at $E_{beam}=370.9$ MeV. The count rate of the focal plane detectors depends on the beam energy and the parameter setting of the JAERI-RMS, and the typical value was 0.5–4 cps for ^{28}Si+^{198}Pt and 50–200 cps for ^{76}Ge+^{150}Nd. The events which fell in the region of interest were selected and used in the data analysis in order to remove the chance

TABLE III. Experimental results of fission cross section for ^{28}Si + ^{198}Pt.

$E_{c.m.}$ [MeV]	σ [mb]	Error [mb]
166.3	789	121
150.0	625	94
140.0	456	68
130.0	204	31
124.6	95.3	14.3
122.0	40.7	6.1
119.6	23.1	3.5
119.0	15.4	2.3
118.0	12.1	1.7
116.9	5.2	0.8
114.9	1.3	0.2

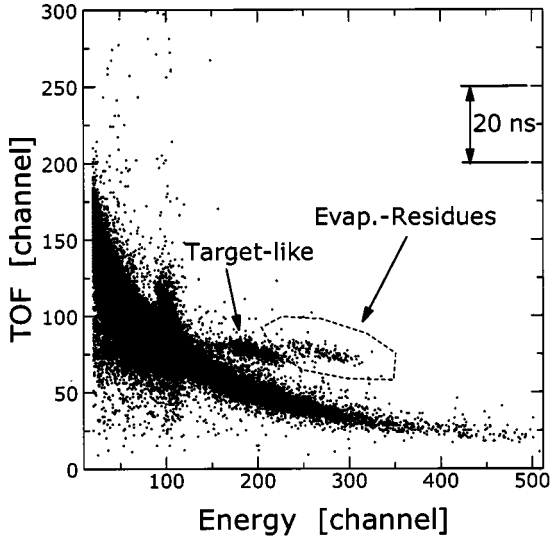

FIG. 5. Two-dimensional spectrum of the time of flight and energy for particles detected in the focal plane detectors of the JAERI-RMS for ^{76}Ge+^{150}Nd. The corresponding beam energy is 370.9 MeV. For the ordinate, 50 channels correspond to 20 ns. The cluster formed by the evaporation residues is encircled with a dashed curve. Targetlike nuclei are observed.

coincidence between background particles and α decay.

Figure 6 shows the typical energy spectra of α decay for ^{28}Si+^{198}Pt obtained at $E_{c.m.}=130.0$ MeV (top) and 147.5 MeV (bottom). This spectrum was obtained by selecting the events having no TOF response. Known α lines are clearly observed in this figure. Some α lines corresponding to successive α decays are observed in Fig. 6. An illustration is found in 130.0 MeV spectrum, where the number of events in the ^{214}Ra peak is comparable with that in the daughter nucleus, ^{210}Rn.

The time difference between the ER implantation and the α_1 decay, namely, the lifetime of α_1-decaying nucleus (τ_1), was used to improve the accuracy of the ER identification.

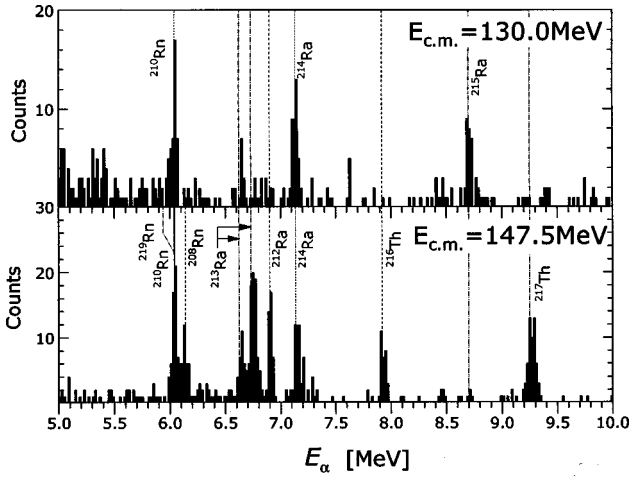

FIG. 6. Spectra of α-partice energy for ^{28}Si+^{198}Pt obtained from the events having no TOF response. The upper and the lower figures are, respectively, obtained at $E_{c.m.}=130.0$ and 147.5 MeV.

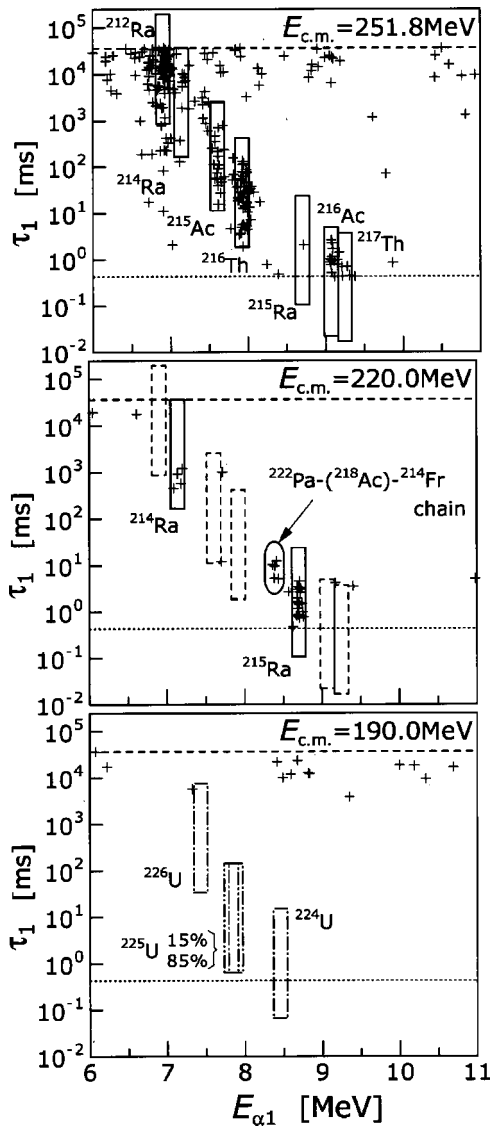

FIG. 7. Events of ER-α_1 correlation plotted on the plane of α energy ($E_{\alpha 1}$) and time interval (τ_1) for ^{76}Ge+^{150}Nd. The three figures correspond to the c.m. energy of 251.8 MeV (top), 220.0 MeV (middle), and 190.0 MeV (bottom). Correlated events having known α lines are surrounded by boxes having ± 90 keV energy gate and the time span of $\frac{1}{15}T_{1/2} \sim 15T_{1/2}$. The solid box means the detection of ER-α_1 events. For $E_{c.m.}=220.0$ MeV, events arising from the ^{222}Pa-(^{218}Ac)-^{214}Fr chain are observed.

Examples of the two-dimensional spectra of $E_{\alpha 1}$ and τ_1 are shown in Fig. 7 obtained for ^{76}Ge+^{150}Nd at $E_{c.m.}=251.8$, 220.0, and 190.0 MeV. In these spectra, the implanted position of ER and the α_1 decay position agreed within $(\Delta X, \Delta Y)=(0.5,0.5)$ mm, and the corresponding energy and TOF channels of the ER fell in the gate on the (E,TOF) spectrum (similar to Fig. 5). The boxes shown in Fig. 7 represent a region around the known α-decay character [15]. It has the energy width of ± 90 keV around the known $E_{\alpha 1}$ and the time span of $\frac{1}{15}T_{1/2} \leqslant \tau_1 \leqslant 15T_{1/2}$. For the spectrum of $E_{c.m.}=190.0$ MeV, we obtained no events in 425 μs$<\tau_1<2$ s. Note that 425 μs shown by the horizontal dotted line corresponds to the dead time of the data acquisition system used for the ^{76}Ge+^{150}Nd experiment, and the horizontal dashed line is $\tau_1=37$ s, over which the chance coincidence becomes much more significant. The production cross sections of ^{217}Th, ^{216}Ac, ^{215}Ra, ^{216}Th, ^{215}Ac, and ^{214}Ra were determined by counting the events in the corresponding boxes. For the ER-^{217}Th correlation in the ^{76}Ge+^{150}Nd experiment, the probability of detecting the ER-^{217}Th event became 31%, which was corrected for in the analysis. Similar correction was made for the channels of ER-^{216}Ac (41%), ER-^{215}Ra (83%), and ER-^{224}U (74%).

In order to confirm the present identification of the α-decay nuclei, we also checked and observed the correlated chain ER-α_1-α_2 for ER-^{217}Th-^{213}Ra, ER-^{216}Th-^{212}Ra, ER-^{214}Ra-^{210}Rn, ER-^{216}Ac-^{212}Fr, and ER-^{215}Ac-^{211}Fr. The α energy agrees with the known value [15] within 90 keV and the lifetime τ is in $\frac{1}{15}T_{1/2} \leqslant \tau \leqslant 15T_{1/2}$. The position agreement is achieved in $(\Delta X, \Delta Y)=(0.5, 0.5)$ mm. We could not observe any ER-^{215}Ra-^{211}Rn chain clearly because of the much longer half-life of ^{211}Rn (14.6 h).

In addition to the six channels mentioned above, we have observed two kinds of successive channels starting, respectively, from ^{222}Pa and ^{221}Th. The ER-^{222}Pa(α_1)-^{218}Ac(α_2)-^{214}Fr(α_3) events are shown in the $E_{c.m.}=220.0$ MeV spectrum of Fig. 7. The α_2 was not observed because of the short half-life of ^{218}Ac (1.12 μs). Because of the same reason as for ^{218}Ac, the ^{217}Ra was not detected in the chain ER-^{221}Th-^{217}Ra-^{213}Rn.

2. Cross section determination

In order to obtain the absolute cross sections of evaporation residues, the detection efficiencies of various ER's by the JAERI-RMS were estimated according to the procedure described in Ref. [16], where we obtained good agreement between the measured detection efficiency of the JAERI-RMS and that calculated by using a program code based on the ion-optical code GIOS [17]. The efficiency calculation takes into account the following effects. The angular distributions of ER's were estimated by using the statistical model code PACE2 [18]. The multiple scattering of the ER's in the target and the charge reset foil were estimated by the TRIM code [19]. We used the charge state distribution of the ER estimated by Shima *et al.* [20]. The efficiency for xn, pxn, and αxn channels is, respectively, 0.05 ($E_{c.m.}=120$ MeV), 0.03 (135 MeV), and 0.02 (135 MeV) for ^{28}Si+^{198}Pt. For ^{76}Ge+^{150}Nd, the efficiency is larger than that of ^{28}Si+^{198}Pt primarily because of the strong kinetic focusing. Simultaneous transport of ERs having two different charge states also enhances the efficiency. The efficiency for ^{76}Ge+^{150}Nd amounted to 0.20 ($E_{c.m.}=120$ MeV) for αxn channels.

The probability detecting the full α energy in the DPSD is taken into account. It is given by $\epsilon=\frac{1}{2}(1+R_{ER}/R_\alpha)$ with R_{ER} and R_α being the implantation depth of the evaporation residue and the range of the α particles, respectively. The R_{ER} and R_α are determined by the TRIM code. The value of ϵ in the reaction of ^{28}Si+^{198}Pt is around 0.53 for the α decay of ^{217}Th.

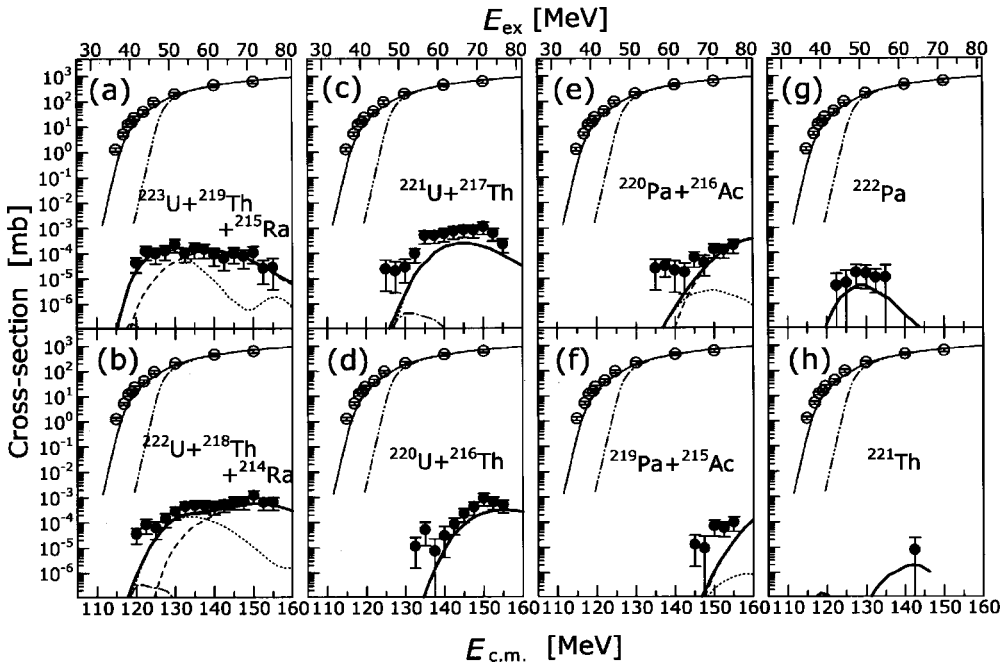

FIG. 8. Fusion and evaporation residue cross sections for ^{28}Si+^{198}Pt as a function of c.m. energy. The excitation energy of the compound nucleus, E_{ex}, is also indicated. Experimental results of *ER* cross sections for the specific channel [(a)–(h)] are shown by solid circles with error bars. The thick solid curve is the results of the statistical model calculation (HIVAP code) coupled with the CCDEF code. For (a)–(f), the cross section includes the components noted in each portion of the figure, and the calculated cross sections of the constituent are shown by the dash-dotted (uranium), dotted (thorium or protactinium), and dashed (radium or actinium) curves. Open circles with error bars plotted in every section are the measured fission cross section shown in Fig. 4. The calculated fusion cross sections based on the coupled channels calculation (thin solid) and the one-dimensional barrier penetration model (thin dash-dot-dotted) are also shown (same as those in Fig. 4).

Evaporation residue cross section is shown in Fig. 8 as a function of c.m. energy for ^{28}Si+^{198}Pt by solid circles with error bars. The data are also listed in Table I. The error includes both statistical contributions and the estimated uncertainty of 50% coming from the transport efficiency of ER's through the JAERI-RMS. The results for ^{76}Ge+^{150}Nd are shown in Fig. 9 and listed in Table II. These figures (tables) include the cross sections determined from the correlation of (a) *ER*-^{215}Ra, (b) *ER*-^{214}Ra, (c) *ER*-^{217}Th, (d) *ER*-^{216}Th, (e) *ER*-^{216}Ac, (f) *ER*-^{215}Ac, (g) *ER*-^{222}Pa, and (h) *ER*-^{221}Th. The cross section determined from the *ER*-^{215}Ra correlation should include the components of $3n$ channel (^{223}U) and $\alpha 3n$ channel (^{219}Th), which cannot be detected in this experiment because of the short half-life of ^{223}U (not known) and ^{219}Th (1.05 μs). For the same reason, the figures in (b)–(f) also include the possible evaporation channels indicated in each figure. The curves in Fig. 8 and Fig. 9 are the theoretical predictions of the cross sections which will be described in the following section.

In the reaction of ^{76}Ge+^{150}Nd, we obtained no correlated *ER*-α_1 event at $E_{c.m.}$=185.0, 190.0, 195.0, and 205.0 MeV, as can be seen in the $E_{c.m.}$=190.0 MeV spectrum of Fig. 7, where no event was detected within the boxes of ^{226}U, ^{225}U, and ^{224}U. In this case we derived the upper limit of the cross section corresponding to one event. The results are listed in Table II, where the upper limits are determined for the nuclei shown in the parentheses.

IV. CALCULATIONS AND DISCUSSIONS

A. Fission cross section for ^{28}Si+^{198}Pt

Since the compound nucleus ^{226}U formed by the reaction ^{28}Si+^{198}Pt is very fissile, the fission cross section can be well approximated to the fusion cross section. The experimental fission cross section shown in Fig. 4 is compared to the calculated fusion cross section based on the coupled channel model [14]. The prediction of the one-dimensional barrier penetration model is shown by a dotted curve, which underestimates the cross section in the region below the Coulomb barrier V_b=126 MeV. The dashed curve is the result of taking into account of the nuclear deformations of ^{198}Pt ($\beta_2=-0.060$ [21], $\beta_4=-0.030$ [22]) and ^{28}Si ($\beta_2=0.407$ [23]). The agreement between the experimental data and the dashed curve is still not satisfactory below $E_{c.m.}$=120 MeV. The solid curve shows the result including the inelastic couplings of the octupole (3^-) vibrational states in ^{28}Si and ^{198}Pt in addition to the nuclear deformation. The deformation parameter β_3 (excitation energy of vibrational state) used in the calculation was 0.398 (6.88 MeV) for ^{28}Si and 0.050 (1.68 MeV) for ^{198}Pt. Since the β_3 value of ^{198}Pt was unknown, we used the value for ^{196}Pt. The CCDEF calculation reproduces the experimental fission cross section quite well.

In Fig. 8, the calculated fusion cross section and the experimental fission cross section are again shown for the convenience of later discussions.

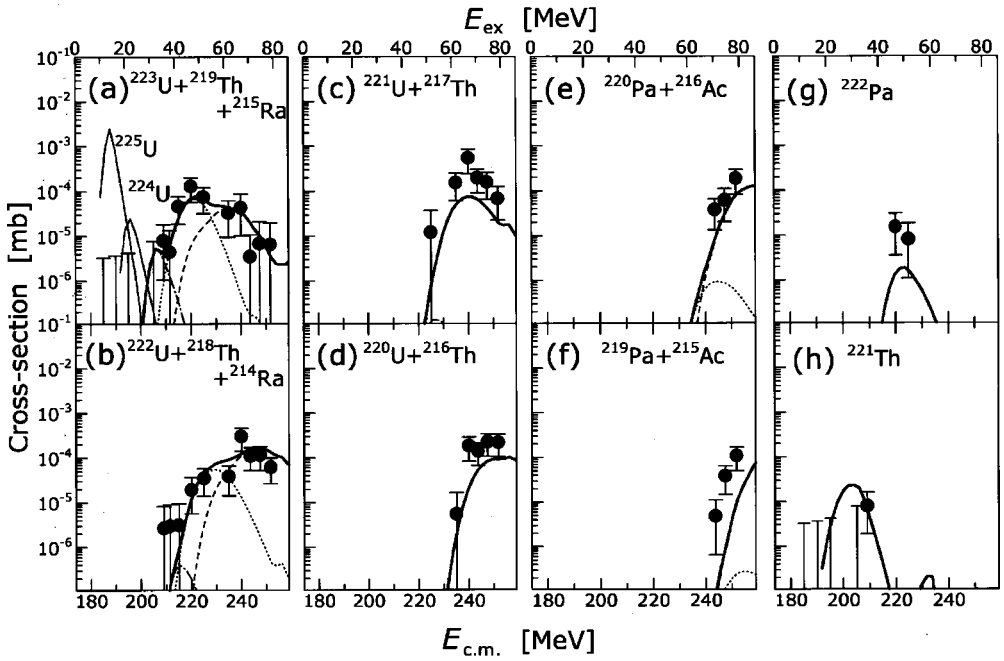

FIG. 9. Evaporation residue cross sections for ^{76}Ge+^{150}Nd as a function of c.m. energy. The excitation energy of the compound nucleus, E_{ex}, is also indicated. The experimental results of *ER* cross sections for the specific channel [(a)–(h)] are shown by solid circles with error bars. In (a) and (h), the upper limit of the *ER* cross section is indicated with the style of error bar (see Table II). The thick solid curve is the results of the statistical model calculation (HIVAP code) coupled with the CCDEF code. The spectra in (a)–(f) include the components noted in each portion of the figure, and the calculated cross sections of the constituent are shown by the dash-dotted (uranium), dotted (thorium or protactinium), and dashed (radium or actinium) curves. In (a), the calculated cross sections for $1n(^{225}\mathrm{U})$ and $2n(^{224}\mathrm{U})$ channels are shown by the thin solid curves.

B. Evaporation residue cross section

The cross section of evaporation residue is calculated by using a statistical model code HIVAP [25] as discussed in this section. The partial wave cross section for fusion was calculated by using the CCDEF code and was input to the HIVAP calculation as the initial spin distribution of the compound nucleus.

A level density of a nucleus at the ground state and at the saddle point used in the analysis is the same as in the previous paper [10], and hence only a summary will be given here. The level density at the ground state as well as the saddle point for a given excitation energy E was calculated by [26,27]

$$\rho(E)=K_{\mathrm{vib}}K_{\mathrm{rot}}\rho_{\mathrm{int}}(E), \tag{3}$$

where K_{vib} is the collective enhancement of the intrinsic level density ρ_{int}, and K_{rot} is the rotational enhancement. The value of K_{vib} (K_{rot}) was set to 1.0 when the quadratic deformation parameter β_2 is larger than 0.17 (less than 0.17) [26]. The β_2 at the ground state was taken from Ref. [22], and the value at the saddle point was taken from Ref. [28]. The level density parameter at the ground state was calculated by

$$a=\tilde{a}\left[1+\{1-\exp(-E/E_{\mathrm{sd}})\}\frac{\delta W}{E}\right], \tag{4}$$

which involves the shell correction energy δW and shell damping energy E_{sd}. The δW was estimated by subtracting from the experimental mass of Ref. [29] the liquid drop mass calculated by Ref. [30]. The value of E_{sd} was set at 18 MeV [31] in this analysis. With increasing E the level density parameter reaches the asymptotic value $\tilde{a}$ determined by the formula in Ref. [32]. The parameter $\tilde{a}$ is a function of mass number, dimensionless surface area, and integrated curvature of a nucleus. The level density parameter at the saddle point is also calculated by Eq. (4) with the second term being zero. This is because the shell correction at the saddle point of preactinides and actinides is small (the range of 0.5 MeV or even less) [27,32]. The fission barrier height was determined by $B_{\mathrm{f}}=B_{\mathrm{LD}}-\delta W$, where the liquid drop fission barrier B_{LD} was calculated by [28].

Several authors have pointed out [33,34] that the measured xn cross sections in the thorium region near the $N=126$ shell closure were overestimated by the standard statistical model calculation. In order to obtain good agreement between the experimental data and the calculation, the shell effect in the level density must be destroyed at unexpectedly low excitation energies; that is, the shell damping factor E_{sd} is taken to be small ($E_{\mathrm{sd}}=6$ MeV^{-1}). This problem was solved by Junghans *et al.* [26] by properly taking into account the collective enhancement of the level density for deformed nucleus. In the present statistical model calculation, we took into account the collective enhancement of the

level density in Eq. (3) and checked how the present calculation reproduced the measured evaporation residue cross sections in the fusion reactions of ^{40}Ar+^{176,178,180}Hf [33]. We obtained good agreement of the calculation with the data within a factor of 2–3 for every xn ($x=2-7$) and pxn ($x=2-5$) channels. For αxn ($x=2-5$) channels, agreement within the factor of 2–5 was achieved. The present calculation also reproduces the ER cross sections for xn ($x=3,4$), pxn ($x=2-5$), and αxn ($x=1-3$) channels following the fusion of ^{32}S+^{182}W [10].

1. ^{28}Si+^{198}Pt

The calculated evaporation residue cross sections are shown in Fig. 8. The cross section of the xn channel (uranium) forms a minor component in the spectra of Figs. 9(a), 9(b), 9(c), and 9(d) (dash-dotted curve).

It is evident in Fig. 8(a) that the calculated cross section for the ^{223}U+^{219}Th+^{215}Ra channel (thick solid curve) increases with $E_{\mathrm{c.m.}}$ and reaches the maximum at 130 MeV and then decreases slowly. This trend is consistent with the experimental data. The magnitude of the cross section also reproduces the experimental data quite well.

The calculated cross section of ^{222}U+^{218}Th+^{214}Ra channel in Fig. 8(b) agrees with the experimental data. The calculation reproduces well the two predominant components of ^{218}Th and ^{214}Ra.

Experimental data of the ^{221}U+^{217}Th channel in Fig. 8(c) and those of the ^{222}Pa channel in Fig. 8(g) have the maximum yield at 145 MeV and 130 MeV, respectively, which is reasonably well reproduced by the calculation. For the former channel, the cross section by the HIVAP calculation is about 5 times lower than the measured value, while the calculation agrees within the the experimental error with the ^{222}Pa data.

The measured cross section for the ^{220}U+^{216}Th channel in Fig. 8(d) increases sharply with $E_{\mathrm{c.m.}}$ above 135 MeV. The sharp increase starts at 140 MeV in the ^{220}Pa+^{216}Ac spectrum of Fig. 8(e). These threshold energies are well reproduced by the calculation. The absolute values are also consistent between the calculation and the experiment. For the channel of ^{219}Pa+^{215}Ac in Fig. 8(f) the threshold energy of 145 MeV are reproduced by the calculation. The calculated cross section is the 5–10 times smaller than the data.

We obtained only one correlated ER-^{221}Th chain at $E_{\mathrm{c.m.}}=142.5$ MeV (Fig. 8(h)). This energy corresponds to the maximum cross section in the HIVAP calculation.

It is worth mentioning that we have detected the evaporation residues below the spherical Coulomb barrier 126 MeV as Fig. 8(a) and Fig. 8(b), which indicates that there is a fusion enhancement relative to the one-dimensional barrier penetration model.

2. ^{76}Ge+^{150}Nd

We show in Fig. 10(a) the calculated fusion cross section by the CCDEF code. The dotted curve is the prediction by the one-dimensional barrier penetration model. The corresponding Coulomb energy is $V_{\mathrm{b}}=209$ MeV. The solid curve in Fig. 10(a) is the calculation that takes into account the target deformation of $(\beta_2,\beta_4)=(0.358, 0.107)$ [21,22]. It also includes the couplings to inelastic channels of the projectile and target. For ^{76}Ge, the deformation parameters (excitation energy) of the quadrupole and octupole vibrations are $\beta_2=0.27$ (0.56 MeV) [37] and $\beta_3=0.14$ (2.69 MeV) [24], respectively. The $\beta_3=0.11$ (0.93 MeV) [24] was adopted for the octupole vibration of ^{150}Nd. As a result of the largely deformed prolate shape of ^{150}Nd [see the inset in Fig. 10(b)], the Coulomb energy varies significantly with the colliding angle θ_{coll} as shown by the solid curve in Fig. 10(b). It results in a large enhancement of the fusion cross section below the spherical Coulomb barrier V_{b}.

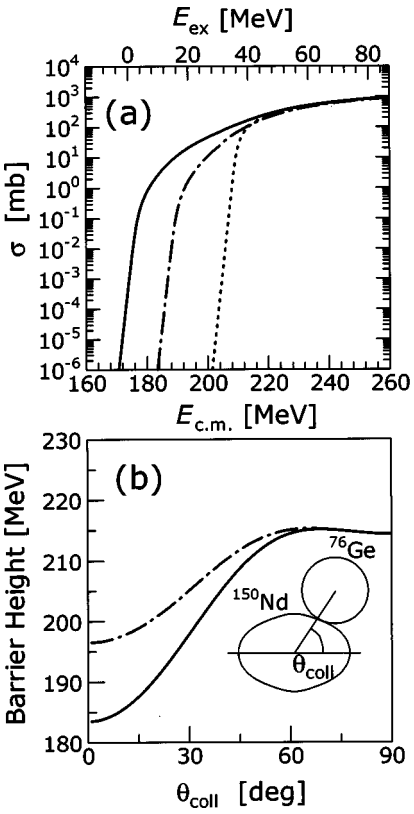

FIG. 10. (a) Calculated fusion cross section based on the coupled channel calculation (solid line) for ^{76}Ge+^{150}Nd. The dotted curve is the prediction by the one-dimensional barrier penetration model. The dash-dotted curve is the result of the coupled channel calculation which includes the effects similar to the solid curve. The difference is, however, that its fusion barrier height has a gain of Eq. (5). (b) Coulomb barrier height plotted as a function of colliding angle θ_{coll}. The solid curve is the original one determined from the CCDEF code. The increase of Eq. (5) with $E_{\mathrm{XX0}}=13$ MeV in the fusion barrier height leads to the dash-dotted curve.

The calculated evaporation residue cross section for ^{76}Ge+^{150}Nd is shown in Fig. 9. The conspicuous feature found in the calculation is the prediction of strongly populated $1n$ and $2n$ channels shown by the thin solid curve in Fig. 9(a), which does not appear in the ^{28}Si+^{198}Pt reaction. This is because the compound nucleus produced in the energy region of $E_{\mathrm{c.m.}}=180-200$ MeV for ^{76}Ge+^{150}Nd has a low excitation energy of 6–26 MeV that would lead to $1n$ and $2n$ final channels.

The calculated evaporation residue cross section in Fig. 9 for (a) ^{223}U+^{219}Th+^{215}Ra, (b) ^{222}U+^{218}Th+^{214}Ra, (d) ^{220}U+^{216}Th, and (e) ^{220}Pa+^{216}Ac reproduces well the experimental data above $E_{\mathrm{c.m.}}\sim 210$ MeV within the error with regard to the absolute value of the cross section and the energy-dependent behavior. Although the calculation underestimates the cross section by about a factor of 5–10 for the channels of (c) ^{221}U+^{217}Th and (f) ^{219}Pa+^{215}Ac, these shapes of the excitation function are very close with each other. The trend of the ^{221}U+^{217}Th and ^{219}Pa+^{215}Ac channels is similar to the ^{28}Si+^{198}Pt reaction. The events of ^{222}Pa were obtained at $E_{\mathrm{c.m.}}=220.0$ and 225.0 MeV at which the calculation yields the maximum cross section in this channel. For ^{221}Th channel, the data point at $E_{\mathrm{c.m.}}=209.0$ MeV agrees with the calculation, whereas no event was detected in $E_{\mathrm{c.m.}}<205$ MeV.

A large difference between the calculation and the experiment is found in the ^{225}U channel. The calculation predicts the cross section of $\sim 1\times 10^{-3}$ mb at 185–190 MeV. However, no event was detected in this energy region, and the upper limit of the cross section was about 3–4 nb. This will be discussed in the following subsection.

C. Extra-extra-push energy in the fusion of ^{76}Ge+^{150}Nd

Good agreement between the experimental results and the HIVAP calculation was achieved for the channels of ^{223}U +^{219}Th+^{215}Ra, ^{222}U+^{218}Th+^{214}Ra, ^{220}U+^{216}Th, and ^{220}Pa+^{216}Ac above $E_{\mathrm{c.m.}}\sim 210$ MeV for the ^{76}Ge+^{150}Nd fusion reaction. In the region of $E_{\mathrm{c.m.}}\geqslant V_{\mathrm{b}}$ (209 MeV) which was dominated by these channels, the fusion reaction of ^{76}Ge+^{150}Nd is explained by the ''standard'' picture; namely, the system fuses completely when it overcomes the Coulomb barrier. In the channels of ^{221}U+^{217}Th and ^{219}Pa +^{219}Ac, the HIVAP calculation predicts a lower cross section than the experimental data, which is similar to the ^{28}Si +^{198}Pt reaction. We consider that the disagreement is attributed to the parameters used in the statistical model calculation which cannot fully imitate the deexcitation process.

On the contrary, below the spherical Coulomb barrier (V_{b}) energy the evaporation residue cross section for ^{76}Ge +^{150}Nd shows anomalous behavior; namely, the cross section of ^{225}U is far below the HIVAP prediction. No α decay was observed for this channel as illustrated in Fig. 7. This discrepancy is attributed to the entrance channel (fusion process) since the deexcitation process appears to be well demonstrated by the statistical model calculation in the ^{28}Si +^{198}Pt reaction which forms the same compound nucleus ^{226}U. The fusion hindrance implied by the ^{225}U cross section is about $1\times 10^{2}\sim 1\times 10^{3}$ in the region of $184<E_{\mathrm{c.m.}}<193$ MeV, suggesting the existence of the extra-extra-push energy.

Although the ^{225}U and ^{224}U channels were not observed in ^{28}Si+^{198}Pt because of the excitation energy of the compound nucleus ^{226}U being larger than 40 MeV in this measurement, we consider that the current statistical model calculation can be applicable in the low excitation region of 10–30 MeV populating the ^{225}U and ^{224}U with a reasonable accuracy from the following consideration. We calculated the ratio $\Gamma_{\mathrm{n}}/\Gamma_{\mathrm{f}}$ of the neutron emission width to the fission width for uranium isotopes having excitation energy of $1n$ channel, and the result was compared with those in Refs. [35,36]. The calculation underestimated the experimental $\Gamma_{\mathrm{n}}/\Gamma_{\mathrm{f}}$ values by the factor of 2 for the compound nuclei $^{232-236}$U, while it reproduced the mass-dependent behavior of the $\Gamma_{\mathrm{n}}/\Gamma_{\mathrm{f}}$ value. The calculation may underestimate the cross section of ^{225}U and ^{224}U in the reaction ^{76}Ge+^{150}Nd by the factor of 2 and 4, respectively. We believe that the calculation does not overestimate the cross sections of ^{225}U and ^{224}U.

We made a rough estimate of the extra-extra-push energy E_{XX} for the ^{76}Ge+^{150}Nd fusion reaction. For a reaction using deformed targets, it is a reasonable assumption that the E_{XX} depends on the colliding angle θ_{coll} because the Coulomb barrier height varies with θ_{coll}. The good agreement between the experimental data and the calculation above $E_{\mathrm{c.m.}}=210$ MeV suggests that no extra-extra-push energy is required above this energy. From the solid curve in Fig. 10(b), the collision with $\theta_{\mathrm{coll}}>\sim 50°$, occupying 65% in solid angle, results in the normal fusion with $E_{\mathrm{XX}}=0$ MeV. In the region of $E_{\mathrm{c.m.}}<\sim 200$ MeV, the collision that can overcome the Coulomb barrier is limited to the near tip collision, the ones of ^{76}Ge with the tip of the prolately deformed ^{150}Nd. The present data show that the system starting from this configuration cannot fuse together with this bombarding energy and an additional kinetic energy E_{XX} is needed to drive the system into the compound nucleus. Here, we introduce the E_{XX} as

$$E_{\mathrm{XX}}(r)=E_{\mathrm{XX0}}\frac{r-R_{\mathrm{side}}}{R_{\mathrm{tip}}-R_{\mathrm{side}}}. \tag{5}$$

The Coulomb barrier distance r is a function of colliding angle θ_{coll} and the distance for the side collision is $R_{\mathrm{side}}=11.7$ fm for ^{76}Ge+^{150}Nd. For the tip collision ($R_{\mathrm{tip}}=14.6$ fm), the above formula gives the extra-extra-push energy of E_{XX0}. Equation (5) comes from the assumption that the more the barrier distance is far away, the additional energy to drive the system into the compound nucleus shape scales with the distance between centers, r, at the Coulomb barrier.

The barrier height was raised to an amount determined by Eq. (5) from the original Coulomb barrier height. The calculated results are shown in Fig. 11 by solid curves. They were obtained with E_{XX0} being 13 MeV as reasonable consistency between the experimental results and the calculations is achieved. The corresponding fusion cross section as a function of $E_{\mathrm{c.m.}}$ is shown in Fig. 10(a) by the dash-dotted curve, and the dependence of the barrier height on the colliding angle is shown Fig. 10(b). The dotted curves in Fig. 11 are the calculations without fusion hindrance, which were already shown in Fig. 9. By including the extra-extra-push energy, the cross section of ^{225}U is reduced to about one-hundredth of the value at the peak cross section. The reduction factor for ^{224}U is about $\frac{1}{4}$. A slight decrease of the cross section of ^{221}Th is found for $E_{\mathrm{c.m.}}<205$ MeV. This calculation gives almost no change in the other ER cross sections

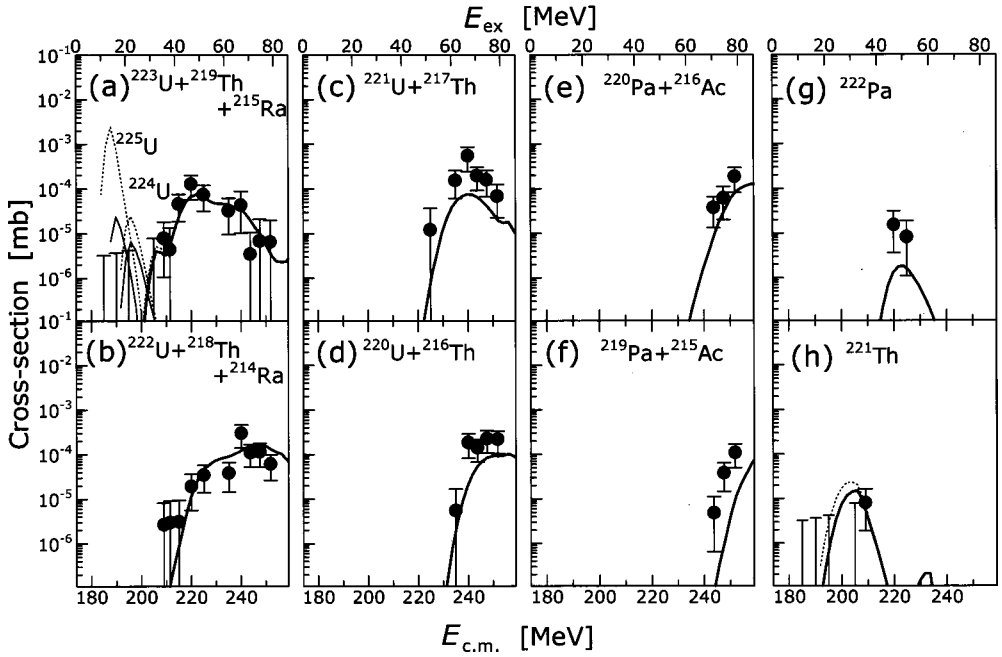

FIG. 11. Same as Fig. 9. The dotted curve is the calculated results using the HIVAP code assuming no extra-extra-push energy (same as the solid curves in Fig. 9). One obtains the solid curve when the fusion cross section shown by the dash-dotted curve in Fig. 10(a) is adopted.

positioned at $E_{c.m.} > \sim 210$ MeV. Reasonable agreement between the calculation and the experiment was also obtained even when we adopt an extremely large value of E_{XX0}, 50 MeV, for instance. This is because the fusion cross section for $E_{c.m.} > \sim 210$ MeV is dominated by the side collision that occupies 65% in solid angle and hence the effect of the fusion hindrance at or near the tip collision is negligible in this energy region. The present analysis can only determine the lowest limit of E_{XX0}, and our choice was 13 MeV for this in the fusion of ^{76}Ge+^{150}Nd.

Our previous work revealed in the ^{60}Ni+^{154}Sm reaction that there is an extra-extra-push energy of 20 MeV at the tip collision. This is larger than 13 MeV for the fusion of ^{76}Ge+^{150}Nd which has a slightly larger effective fissility parameter than ^{60}Ni+^{154}Sm. However, it must be noted that the E_{XX0} value obtained in the present work is the lowest limit of the extra-extra-push energy at the tip collision. The common conclusion reached through the study of ^{76}Ge +^{150}Nd and ^{60}Ni+^{154}Sm is that there is no fusion hindrance at the side collision in these systems.

The present conclusion was the same with that in Refs. [38,39] by Hinde *et al*. In the measurement of fission anisotropy (and also mass distribution [39]) for ^{16}O+^{238}U, they gave an interpretation that collisions of ^{16}O with the tip of prolately deformed ^{238}U nuclei result in quasifission in the sub-barrier energy region, while collisions with the side result in fusion. The same discussion was made in the reaction ^{12}C+^{232}Th [40]. The effective fissility parameters χ_{eff} for ^{16}O+^{238}U and ^{12}C+^{232}Th are 0.463 and 0.390, respectively, and are far below the threshold $\chi_{eff}=0.750$. However, the systematic of Ref. [9] predicting E_{XX} versus χ_{eff} does not include the data taken from the evaporation residue cross section using actinide nuclei.

V. SUMMARY AND CONCLUSIONS

Evaporation residue cross sections for ^{28}Si+^{198}Pt and ^{76}Ge+^{150}Nd, both of which form a compound nucleus ^{226}U, were measured in the vicinity of the Coulomb barrier. The measurement gave direct evidence that the system fuses together to form a fully equilibrated compound nucleus.

For ^{28}Si+^{198}Pt, we have obtained the fusion cross section from measurement of the fission fragment angular distribution by taking advantage of the high fissility of ^{226}U. The fusion cross section for ^{28}Si+^{198}Pt agrees well with the prediction by the coupled channel calculation which takes into account the nuclear deformation effects and the couplings to inelastic channels.

The statistical model calculation (HIVAP code) nicely reproduced the evaporation residue cross section of ^{28}Si +^{198}Pt. It should be noted that the parameters we have used in the HIVAP code are the same for both reactions studied here as well as in studies of the previous reactions of ^{32}S +^{182}W and ^{60}Ni+^{154}Sm [10].

Considering the same compound nucleus ^{226}U formed by ^{76}Ge+^{150}Nd and the same way of deexcitation as ^{28}Si +^{198}Pt, the evaporation residue cross section for ^{76}Ge +^{150}Nd allowed us to study the fusion process (entrance channel) of this reaction. Assuming that the partial wave fusion cross section for ^{76}Ge+^{150}Nd is predicted by the CCDEF code, the evaporation residue cross section agrees well with the statistical model calculation for $E_{c.m.} > \sim 210$ MeV. Since the cross section for $E_{c.m.} > \sim 210$ MeV is dominated by the side collision, the results suggested no fusion hindrance in this way of collision. On the contrary, in the region of $184 < E_{c.m.} < 193$ MeV, there was a fusion hindrance of $1\times10^{2} \sim 1\times10^{3}$ compared to the fusion cross sec-

tion calculated by the CCDEF code, indicating that the extra-extra-push energy is required for the system to fuse together when the fusion starts from the specific configuration that ^{76}Ge collides with the tip of ^{150}Nd. By assuming the extra-extra-push energy to be proportional to the Coulomb barrier distance, we obtained 13 MeV as the lowest limit of extra-extra-push energy for the tip collision.

It is known that the extra-extra-push energy increases with the effective fissility parameter above the threshold of $\chi_{\mathrm{eff}}=0.75$. With this respect it is reasonable that in the ^{76}Ge+^{150}Nd system with $\chi_{\mathrm{eff}}=0.749$ there is an extra-extra-push energy to a certain extent. In our previous work in [10], the fusion hindrance for the tip collision was observed in the reaction ^{60}Ni+^{154}Sm. The conclusion reached through the two reactions is that there is no fusion hindrance at the side collision for these systems. It would be interesting to investigate the existence of extra-extra-push energy for the side collision in a system having larger χ_{eff} value, and we are planning to make such an experiment.

ACKNOWLEDGMENTS

The authors thank the crew of the JAERI tandem-booster facility for the beam operation.

[1] Yu.Ts. Oganessian, V.K. Utyonkov, Yu.V. Lobanov, F.Sh. Abdullib, A.N. Polyakov, I.V. Shirokovsky, Yu.S. Tsyganov, G.G. Gulbekian, S.L. Bogomolov, B.N. Gikal, A.N. Mezentsev, S. Iliev, V.G. Subbotin, A.M. Sukhov, G.V. Buklanov, K. Subotic, M.G. Itkis, K.J. Moody, J.F. Wild, N.J. Stoyer, M.A. Stoyer, and R.W. Lougheed, Phys. Rev. Lett. **83**, 3154 (1999).
[2] V. Ninov, K.E. Gregorich, W. Loveland, A. Ghiorso, D.C. Hoffman, D.M. Lee, H. Nitsche, W.J. Swiatecki, U.W. Kirback, C.A. Laue, J.L. Adams, J.B. Patin, D.A. Shaughnessy, D.A. Strellis, and P.A. Wilk, Phys. Rev. Lett. **83**, 1104 (1999).
[3] W. Nörenberg, in Proceedings of the International Workshop on Heavy-Ion Fusion, Padua, Italy, 1994.
[4] A. Iwamoto, P. Möller, J.R. Nix, and H. Sagawa, Nucl. Phys. **A596**, 329 (1996).
[5] J.R. Leigh, M. Dasgupta, D.J. Hinde, J.C. Mein, C.R. Morton, R.C. Lemmon, J.P. Lestone, J.O. Newton, H. Timmers, J.X. Wei, and N. Rowley, Phys. Rev. C **52**, 3151 (1995).
[6] M. Dasgupta, D.J. Hinde, J.R. Leigh, and K. Hagino, Nucl. Phys. **A630**, 78c (1998).
[7] M. Beckerman, Rep. Prog. Phys. **51**, 1047 (1988).
[8] S. Bjørnholm and W.J. Swiatecki, Nucl. Phys. **A391**, 471 (1982).
[9] H. Gäggeler, T. Sikkeland, G. Wirth, W. Brüchle, W. Bögl, G. Franz, G. Herrmann, J.V. Kratz, M. Schädel, K. Sümmerer, and W. Weber, Z. Phys. A **316**, 291 (1984).
[10] S. Mitsuoka, H. Ikezoe, K. Nishio, and J. Lu, Phys. Rev. C (submitted).
[11] H. Ikezoe, Y. Nagame, T. Ikuta, S. Hamada, I. Nishinaka, and T. Ohtsuki, Nucl. Instrum. Methods Phys. Res. A **376**, 420 (1996).
[12] V.E. Viola, K. Kwiatkowski, and M. Walker, Phys. Rev. C **31**, 1550 (1985).
[13] B.B. Back, R.R. Betts, J.E. Gindler, B.D. Wilkins, S. Saini, M.B. Tsang, C.K. Gelbke, W.G. Lynch, M.A. McMahn, and P.A. Baisden, Phys. Rev. C **32**, 195 (1985).
[14] J.O. Fernández Niello, C.H. Dasso, and S. Landowne, Comput. Phys. Commun. **54**, 409 (1989).
[15] R.B. Firestone, in *Table of Isotopes*, edited by V.S. Shirley (Wiley, New York, 1996).
[16] T. Kuzumaki, H. Ikezoe, S. Mitsuoka, T. Ikuta, S. Hamada, Y. Nagame, I. Nishinaka, and O. Hashimoto, Nucl. Instrum. Methods Phys. Res. A **437**, 107 (1999).
[17] H. Wollnik, J. Brezina, and M. Berz, Nucl. Instrum. Methods Phys. Res. A **258**, 408 (1987).
[18] A. Gavron, Phys. Rev. C **21**, 230 (1980).
[19] J.F. Ziegler, J.P. Biersack, and U. Littmark, *The Stopping and Range of Ions in Solids* (Pergamon, New York, 1985).
[20] K. Shima, T. Ishihara, and T. Mikuno, Nucl. Instrum. Methods Phys. Res. **200**, 605 (1982).
[21] P. Raghavan, At. Data Nucl. Data Tables **42**, 189 (1989).
[22] P. Möller, J.R. Nix, W.D. Myers, and W.J. Swiatecki, At. Data Nucl. Data Tables **59**, 185 (1995).
[23] M. Dasgupta, A. Navin, Y.K. Agarwal, C.V.K. Baba, H.C. Jain, and M.L. Jhingan, Nucl. Phys. **A539**, 351 (1992).
[24] R.H. Spear, At. Data Nucl. Data Tables **42**, 55 (1989).
[25] W. Reisdorf and M. Schädel, Z. Phys. A **343**, 47 (1992).
[26] A.R. Junghans, M. de Jong, H.-G. Clerc, A.V. Ignatyuk, G.A. Kudyaev, and K.-H. Schmidt, Nucl. Phys. **A629**, 635 (1998).
[27] A.S. Iljinov, M.V. Mebel, N. Bianchi, E. De Sanctis, C. Guaraldo, V. Lucherini, V. Muccifora, E. Polli, A.R. Reolon, and P. Rossi, Nucl. Phys. **A543**, 517 (1992).
[28] S. Cohen, F. Plasil, and W.J. Swiatecki, Ann. Phys. (N.Y.) **82**, 557 (1974).
[29] G. Audi and A.H. Wapstra, Nucl. Phys. **A595**, 409 (1995).
[30] W.D. Myers and W.J. Swiatecki, Ark. Fys. **36**, 343 (1967).
[31] A.V. Ignatyuk, G.N. Smirenkin, and A.S. Tishin, Yad. Fiz. **21**, 485 (1975) [Sov. J. Nucl. Phys. **21**, 255 (1975)].
[32] W. Reisdorf, Z. Phys. A **300**, 227 (1981).
[33] D. Vermeulen, H.-G. Clerc, C.-C. Sahm, K.-H. Schmidt, J.G. Keller, G. Munzenberg, and W. Reisdorf, Z. Phys. A **318**, 157 (1984).
[34] C.-C. Sahm, H.-G. Clerc, K.-H. Schmidt, W. Reisdorf, P. Armbruster, F.P. Hessberger, J.G. Keller, G. Münzenberg, and D. Vermeulen, Nucl. Phys. **A441**, 316 (1985).
[35] A. Gavron, H.C. Britt, E. Konecny, J. Weber, and J.B. Wilhelmy, Phys. Rev. Lett. **34**, 827 (1975).
[36] R. Vandenbosch and J.R. Huizenga, *Nuclear Fission* (Academic, New York, 1973), p. 227, see Fig. VII-3.
[37] S. Raman, C.H. Malarkey, W.T. Milner, C.W. Nestor, Jr., and P.H. Stelson, At. Data Nucl. Data Tables **36**, 1 (1987).
[38] D.J. Hinde, M. Dasgupta, J.R. Leigh, J.P. Lestone, J.C. Mein, C.R. Morton, J.O. Newton, and H. Timmers, Phys. Rev. Lett. **74**, 1295 (1995).
[39] D.J. Hinde, M. Dasgupta, J.R. Leigh, J.C. Mein, C.R. Morton, J.O. Newton, and H. Timmers, Phys. Rev. C **53**, 1290 (1996).
[40] J.C. Mein, D.J. Hinde, M. Dasgupta, J.R. Leigh, J.O. Newton, and H. Timmers, Phys. Rev. C **55**, R995 (1997).